

# A 13.56-MHz Wireless Power Transfer System With Enhanced Load-Transient Response and Efficiency by Fully Integrated Wireless Constant-Idle-Time Control for Biomedical Implants

Cheng Huang<sup>ID</sup>, Member, IEEE, Toru Kawajiri, Member, IEEE, and Hiroki Ishikuro, Member, IEEE

**Abstract**—In this paper, a complete wireless power transfer system with transmitter (TX) and receiver (RX) chips is presented. Both RX local and TX wireless output voltage regulations are achieved by the proposed constant-idle-time control without using any wires or additional discrete components, such as MCU, DAC, various kinds of controllers, and decoders, which were required in previous works. The system and circuitry design complexity is significantly reduced. Both TX and RX chips are fabricated in the TSMC 65-nm process with standard 2.5-V I/O devices, and the RX coil is fabricated using flexible printed circuits to demonstrate the performance for implantable applications. Up to 17.5% end-to-end total efficiency improvement is observed when enabling the wireless constant-idle-time controlled TX voltage regulation, and an instant load-transient response is also achieved. As a result, compared to previous works, this design achieves a higher total efficiency, a faster load-transient response, and a higher level of integration with a much lower system and circuitry design complexity.

**Index Terms**—Backscattering, biomedical implants, constant-idle-time, efficiency, flexible printed circuits (FPCs), full integration, load-transient response, voltage regulation, wireless power transfer (WPT).

## I. INTRODUCTION

WIRELESS power transfer systems (WPT) are very popular in bioimplants applications, such as cochlear implants [1], [2], retinal prostheses [3], [4], or brain machine interfaces [5]. Compared to battery supplies, WPT can achieve a smaller form factor and theoretically unlimited lifetime, which is very important for bioimplants because battery replacements may require surgeries. A simple WPT system includes a transmitter (TX), wireless power link, and receiver (RX). The TX extracts the power from a power source, such as a battery, and drives the TX coil using a coil driver, such as a class D amplifier. The power is then

Manuscript received February 28, 2017; revised July 4, 2017; accepted October 20, 2017. Date of publication November 21, 2017; date of current version January 25, 2018. This paper was approved by Associate Editor Michiel A. P. Pertjis. This work was supported by CREST/JST. (Corresponding author: Cheng Huang.)

The authors are with the Department of Electronics and Electrical Engineering, Keio University, Yokohama 223-8522, Japan (e-mail: dootsewhuang@gmail.com; kawajiri@skr.elec.keio.ac.jp; ishikuro@elec.keio.ac.jp).

Color versions of one or more of the figures in this paper are available online at <http://ieeexplore.ieee.org>.

Digital Object Identifier 10.1109/JSSC.2017.2767181

transferred through the wireless link, and picked up by the RX coil in the bioimplant underneath the skin. The received AC voltage is then rectified to a DC voltage to supply the biomedical function circuits. Usually, a well-regulated DC voltage is required for the load to operate, while the voltage provided by the rectifier is highly dependent on various conditions such as the loading variation and coupling conditions, e.g., distance and alignments between the TX and RX coils. The most traditional way to regulate the output voltage  $V_O$  is using an LDO or buck converter as a second stage after the rectifier at the RX side [7], [8], as shown in Fig. 1(a). However, as an extra stage, the efficiency will be degraded. Besides, a dedicated over voltage protection (OVP) is required to protect the devices at the rectifier since the  $V_{REC}$  is not regulated and may reach a voltage higher than the rating of the devices. Single-stage solutions to regulate the voltage inside the rectifier are introduced in [8]–[10], namely, regulating or regulated rectifier, as shown in Fig. 1(b). By switching the rectifier between different configurations, such as 1X and 2X [8], [9], or 0X, 1/2X, and 1X [10], with a feedback controlled duty cycle,  $V_O$  can be regulated without an LDO or buck. It achieves a better efficiency, and OVP may be at the same time ensured by the voltage regulation [10]. Besides the RX voltage regulation, if the TX is not adjusted and always prepared to transfer the maximum power consider worst cases, i.e., longest distance with maximum loading, then the system efficiency, which is defined as the end-to-end efficiency that includes all the power loss in the TX, wireless link, and RX, is not well optimized at normal operation. For many applications, the TX is portable and powered by batteries, so the end-to-end total system efficiency is related to battery life and is also important. To improve the total efficiency over a wide operation range, TX voltage regulation with adjustable transmitted power based on the load or coupling coefficient is necessary. This requires wireless communication between RX and TX, so that the TX is able to receive the information from the RX of how much power RX receives and how much loading it has to adjust the transmitted power. As shown in Fig. 2(a), [7] and [11] use a wire between TX and RX to establish the communication between RX and TX. However, wire is not available in a WPT system. In [3] and [12],

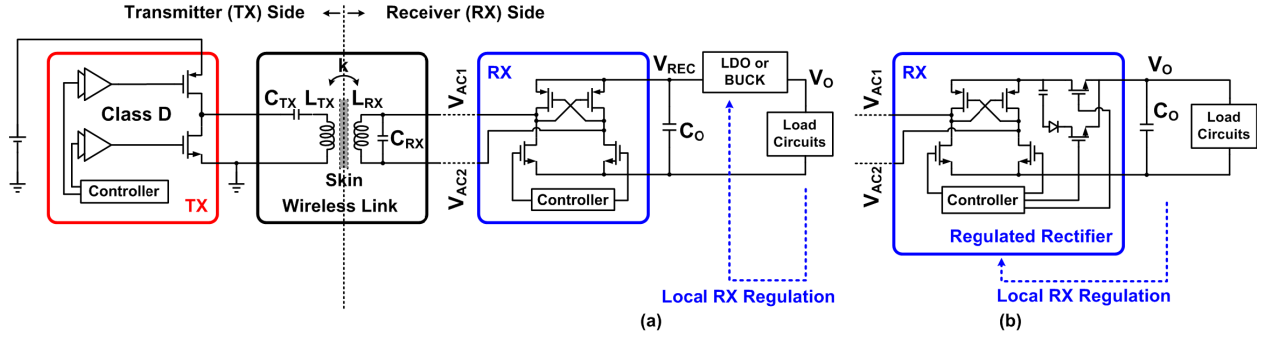


Fig. 1. Examples of WPT systems with local RX voltage regulation realized by (a) extra stage of LDO or buck converter and (b) single-stage regulating rectifier.

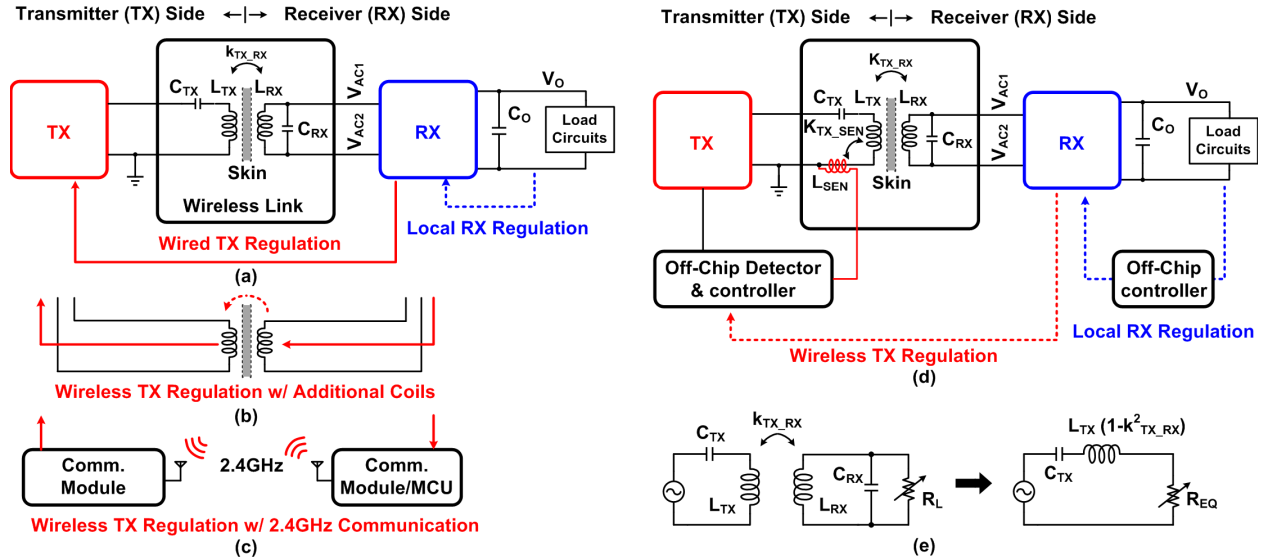


Fig. 2. Examples of WPT systems with TX voltage regulation. Communication link is established by (a) wire, (b) additional pair of coils, (c) 2.4-GHz out-band signals, and (d) backscattering with (e) LSK modulation.

an additional pair of coils is used to establish the wireless data link between RX and TX and can be used for TX regulation, as shown in Fig. 2(b). However, coils are relatively large in size, especially for the RX side, which is an implant. Communication between TX and RX through the 2.4-GHz band is presented in [7] for TX voltage regulation, as shown in Fig. 2(c). However, the system design is highly complicated with communication modules and an MCU. It is also costly and power hungry. The antenna in the RX also results in increase of size. As a result, all the methods introduced above and shown in Fig. 2(a)–(c) are not very suitable for implant applications.

Backscattering, as shown in Fig. 2(d), is introduced for TX voltage regulation in [9], [13], and [14] using the load-shift keying (LSK) methodology. The TX voltage regulation is controlled by the RX with the load changes during the RX voltage regulation. As shown in Fig. 2(e), for a parallel resonant RX, the load  $R_L$  at the RX is reflected to the TX as  $R_{EQ}$  [15]

$$R_{EQ} = \frac{k_{TX\_RX}^2 L_{TX}}{L_{RX}} R_L \quad (1)$$

when  $R_L$  at the RX is changing, the difference will be reflected to the TX as the changes of  $R_{EQ}$ . With the same

input voltage, the current through the  $L_{TX}$  is also changing. By using an additional coil at the TX to sense the  $L_{TX}$  current difference, the LSK signal is then recovered in the TX and the communication between TX and RX can be established. In this way, the power link for TX/RX power transfer can be reused for communication purpose, with the cost of an extra coil at the external TX while the implanted RX is not affected. So this solution is very suitable for biomedical applications. However, the existing designs are highly complicated with a lot of off-chip components, and the dynamic responses are relatively slow. For example, analog signals that contain duty cycle information are transferred from RX to TX in [14]. So off-chip components such as DAC, DAC controller, decoder, and data RX are required. And the adjustment of the transmitted power is achieved by using a buck converter to vary the supply of the class D amplifier, so a discrete power inductor is also used. In [9] and [13], the system and circuitry design complexity is also high with lots of off-chip components such as digital controllers, decodes, pulse generators, and diodes. For these designs, the load-transient response is limited by the system bandwidth, which requires careful modeling and small signal analysis. This can be very challenging due to the high system complexity and various operation conditions with the

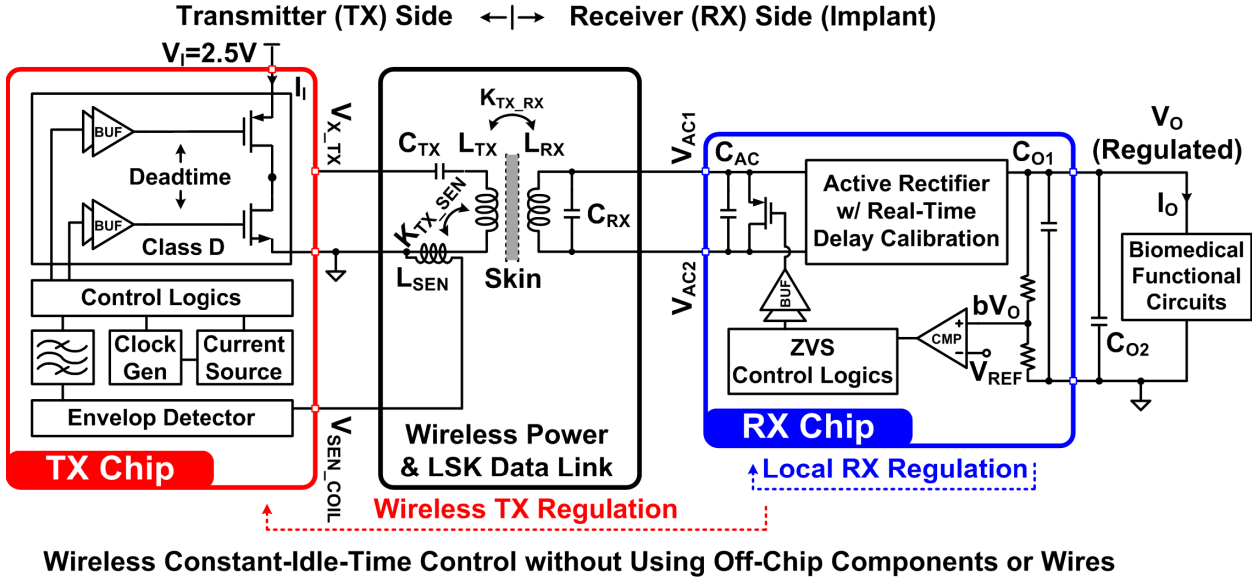


Fig. 3. System block diagram of the proposed WPT system with wireless constant-idle-time control.

wireless link. As a result, dominant-pole compensation is usually implemented to ensure the stability under different conditions, while the bandwidth is not well optimized. So the load-transient recovery time, which is defined as the period from the load-transient happens to  $V_O$  settles again to the steady state, is measured as slow as 40 ms [13] or 2 ms [14]. Although the power consumption by external active components are not included in the efficiency calculation in [9], [13], and [14], it does contribute to the power loss and degrades the total efficiency. Recently, a smart idea to self-adjust the TX frequency to the two split resonant frequencies to achieve regulated RX voltage independent to the coupling and loading conditions without using even a sensing coil but only two 40- $\mu$ H inductors for frequency tuning is presented in [16]. However, the frequency varies from 10.4 to 13.56 MHz due to the nature of operation, while the useable frequencies for WPT system are restricted to the industrial, scientific and medical (ISM) bands [10], [11], [18], [19]. The variation is restricted to 13.553–13.567 MHz for the 13.56-MHz band. So the application of the methodology in [16] may be limited.

In this paper [6], the goal is to reduce the system and circuit design complexity, minimize the number of off-chip components required for both RX local and TX wireless voltage regulation, and at the same time achieve faster load-transient response and higher system efficiency. Section II introduces the proposed constant-idle-time control in detail. Measurement results and conclusions will be given in Sections III and IV, respectively.

## II. PROPOSED WPT SYSTEM WITH FULLY INTEGRATED WIRELESS CONSTANT-IDLE-TIME CONTROL

Fig. 3 shows the system block diagram of the proposed design. It is a complete WPT system that includes two chips: both the TX and RX chips; and three coils: the TX power coil  $L_{TX}$ , TX sensing coil  $L_{SEN}$ , and the RX power coil  $L_{RX}$ .

The constant-idle-time control can be divided into two parts: the RX local voltage regulation; and the TX wireless voltage regulation that is initiated by the RX local regulation using backscattering communication link. No off-chip components other than the coils and capacitors are required for the constant-idle-time control.

### A. Operation Principle of the RX Local Voltage Regulation

Fig. 4 shows the detail circuitry and operation principle of the RX local voltage regulation. The RX chip contains an active rectifier with real-time delay calibration introduced in [17] for better efficiency, and some regulation circuits to regulate  $V_O$  as shown in Fig. 4(b). When the divided output voltage  $bV_O$  is higher than the  $V_{REF}$ , the comparator will be triggered, which indicates the received power is too much for the load. The inputs of the RX,  $V_{AC1}$ , and  $V_{AC2}$ , need to be shorted by  $M_{STOP}$  to reject power transmitted from the TX. While before shorting the inputs of RX, since this may happen randomly at any phase in a switching cycle and is not predictable, if the inputs are shorted at the time when there is a large voltage across the RX resonant capacitor  $C_{AC}$ , the energy stored in  $C_{AC}$  will be lost and the efficiency will be slightly affected. For a better optimization, a rough zero-voltage-switching (ZVS) circuit is used to reduce the energy loss, which will be further explained in detail in Section II-B. It is simply realized by a three-input NAND gate. When the comparator  $V_{CMP}$  is triggered,  $V_{AC1}$  and  $V_{AC2}$  will not be shorted until both  $V_{AC1}$  and  $V_{AC2}$  are high. As a result, the gate is only triggered when the voltage across  $C_{AC}$  is roughly equal, and thus the energy loss of  $C_{AC}$  can be reduced. The ZVS operation is later verified in measurement, as shown in Fig. 4(b). The  $V_{ZVS}$  shown in Fig. 4(b) is the output of the ZVS NAND gate. When it is triggered, the  $M_{STOP}$  will be turned on to short the inputs of the RX. After that, since there is no power received in the RX,  $V_O$  will return to the boundary, and both  $V_{CMP}$  and  $V_{ZVS}$  will return low. However,

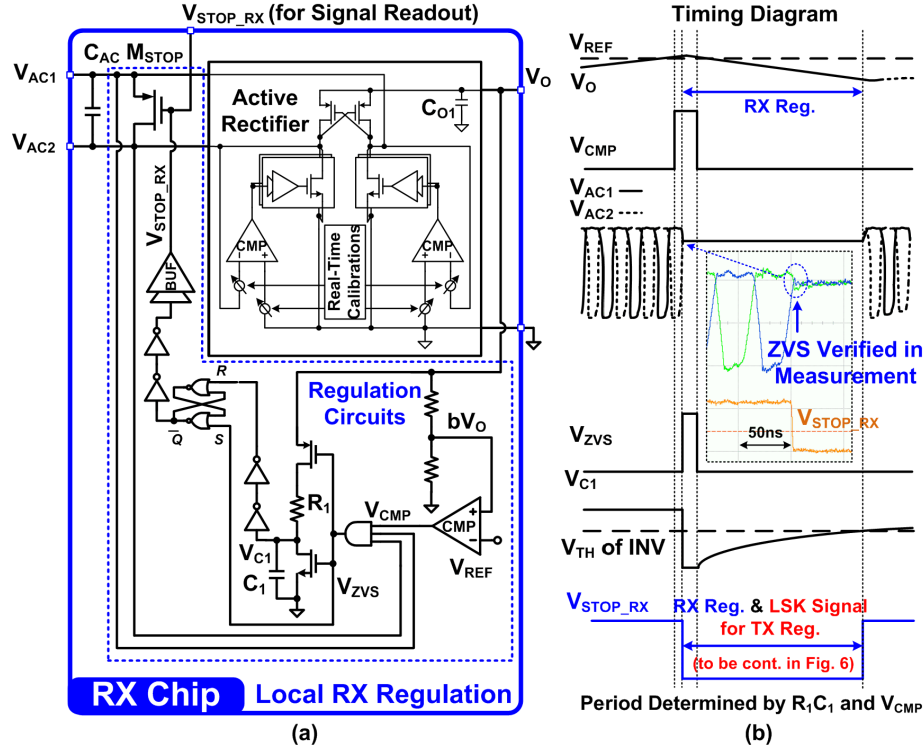


Fig. 4. (a) Detailed circuitry and (b) operation principle of the RX chip of the proposed WPT system.

the  $M_{STOP}$  is latched on until an  $R_1C_1$  delay, which is designed to be  $\sim 500$  ns. It should be long enough to trigger the later wireless TX regulation at the worst coupling coefficient. After  $\sim 500$  ns, the RX will switch again. In this way,  $bV_O$  is regulated to  $V_{REF}$ , and no dedicated OVP is required since the voltages in the RX are bounded by  $V_{REF}$ .

As a single-stage solution to regulate  $V_O$  [8]–[10], [14], higher efficiency is expected. The tradeoff is the higher switching noise, which is directly exposed to the load and not desired for sensitive analog circuits. In this case, high power supply rejection LDOs can be used on demand.

#### B. RX AC Voltages Definition Referring to Ground for ZVS Operation

As introduced in Section II-A, a NAND gate is used to minimize the energy loss by shorting the  $C_{AC}$  only when both  $V_{AC1}$  and  $V_{AC2}$  are high. While in an active rectifier, how the  $V_{AC}$  referring to ground are defined and when they equal are not straightforward since both  $V_{AC1}$  and  $V_{AC2}$  are kind of “floating” and the active diodes only conduct for a short period.

In this paper, NMOS is used as active diode and PMOS as passive diode for better efficiency [17]. To define the  $V_{AC1}$  and  $V_{AC2}$  referring to ground, DC or AC paths are necessary. As shown in Fig. 5, the operation of the active rectifier is divided into four phases. In  $\Phi 1$ , both NMOSs are off, and  $V_{AC1}$  is falling from high to low. When  $V_{AC1}$  drops below  $V_O - V_{tP}$ , in which  $V_{tP}$  is the threshold voltage of the power PMOSs,  $M_{P2}$  is turned on and  $V_{AC2} = V_O$  without IR drops since no current is flowing. After  $V_{AC1}$  falls below zero, which is shown as  $\Phi 2$ ,  $M_{N1}$  is turned on and current is then flowing through  $M_{P2}$  and  $M_{N1}$  to deliver to the output and charge  $C_O$ . Due to the IR drops on  $M_{P2}$  and  $M_{N1}$ ,  $V_{AC1}$  will

be slightly below zero and  $V_{AC2}$  above  $V_O$ . Then, when  $V_{AC1}$  returns to above zero and starts to rise, which is shown as  $\Phi 3$ ,  $M_{N1}$  is turned off to stop the reverse current discharging  $C_O$ .  $M_{P2}$  is still on before  $V_{AC1}$  reaches  $V_O - V_{tP}$ , but since current stops flowing,  $V_{AC2} = V_O$ . From  $\Phi 1$ – $\Phi 3$ ,  $M_{P2}$  is on and  $V_{AC2}$  is always well defined by DC paths. When  $V_{AC1}$  rises above  $V_O - V_{tP}$ , which is shown as  $\Phi 4$ , all four transistors are turned off, leaving only parasitic capacitance as AC paths to define  $V_{AC1}$  and  $V_{AC2}$  referring to ground. So as a result,  $V_{AC1}$  continues to rise and  $V_{AC2}$  starts to drop, and the crossing point is in the middle, which is  $V_O - V_{tP}/2$ . After that,  $V_{AC2}$  continues to drop and the operation of  $\Phi 1$ – $\Phi 4$  repeats with the  $V_{AC1}$  and  $V_{AC2}$  position swapped. As a conclusion, the voltage when  $V_{AC1}$  equals to  $V_{AC2}$  is  $V_O - V_{tP}/2$ . In TSMC 65 nm, the  $V_{tP}$  of minimal width (280 nm) I/O device is 479 mV typically, and 422/535 mV for fast/low corners. So the voltage when  $V_{AC1} = V_{AC2}$  is 211 to 268 mV below  $V_O$ . The green lines in Fig. 5(a) shows how the sinusoidal  $V_{AC1}$ – $V_{AC2}$  differential signal looks like, and what a full-wave rectifier sees by flipping and shifting the voltage. Fig. 5(b) shows the simulation waveforms, which matches well with the explanation. Since the PMOS is design to be large to maximize power conversion efficiency and voltage conversion ratio [17], the IR drops on PMOS is very small. Fig. 5(c) shows the simulated differential signal, and the flipped and shifted signal seen by the full-wave rectifier, which almost overlaps the  $V_{AC1}$  and  $V_{AC2}$  with a slight difference at  $\Phi 4$ . Fig. 5(d) shows the measured results in [17]. So as a result, during  $\Phi 4$ , both  $V_{AC1}$  and  $V_{AC2}$  are high and roughly equal, thus a three-input NAND gate with adjusted PMOS and NMOS strength can be used as a simple solution to achieve ZVS operation.

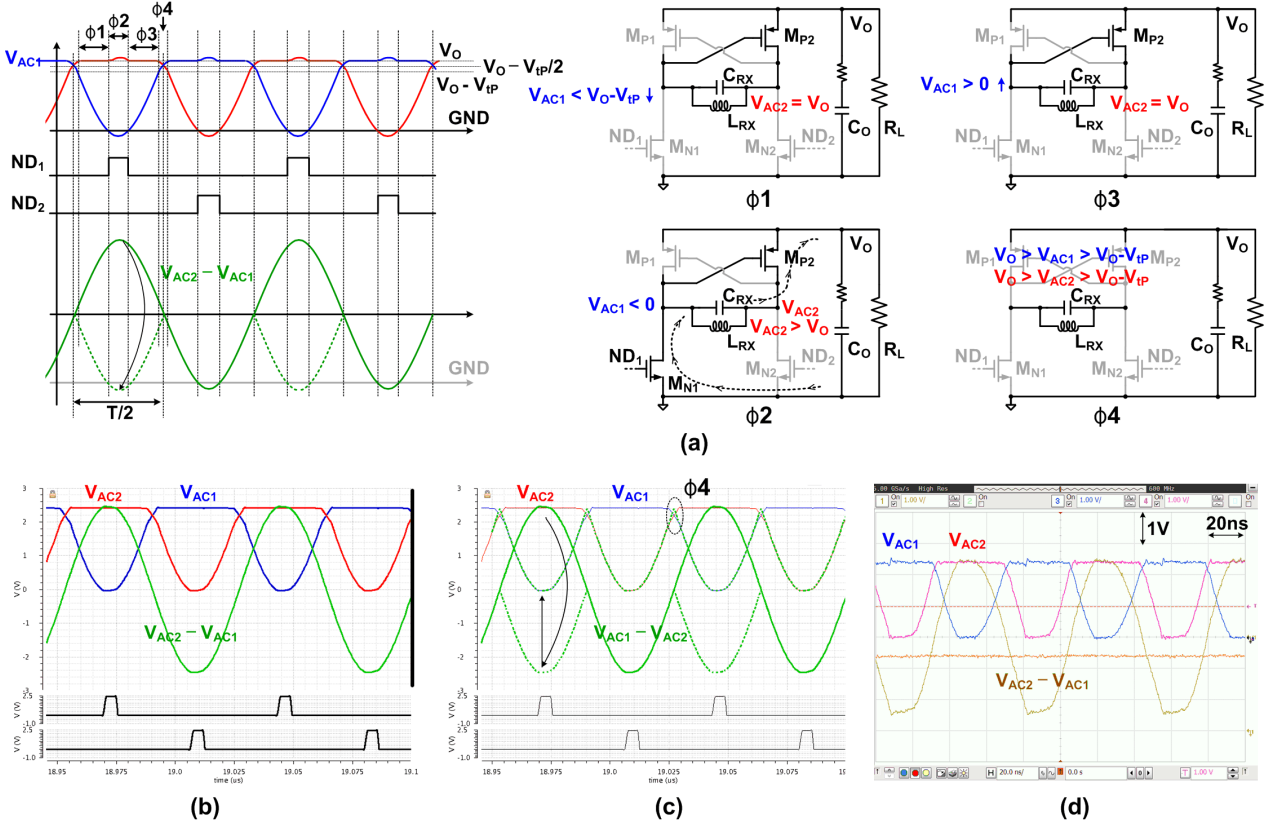


Fig. 5. (a) Illustration of  $V_{AC}$  voltages referring to ground in different operation phases. (b) Simulated waveforms. (c) Flipped and shifted  $V_{AC}$  seen by the rectifier. (d) Measured waveforms [17].

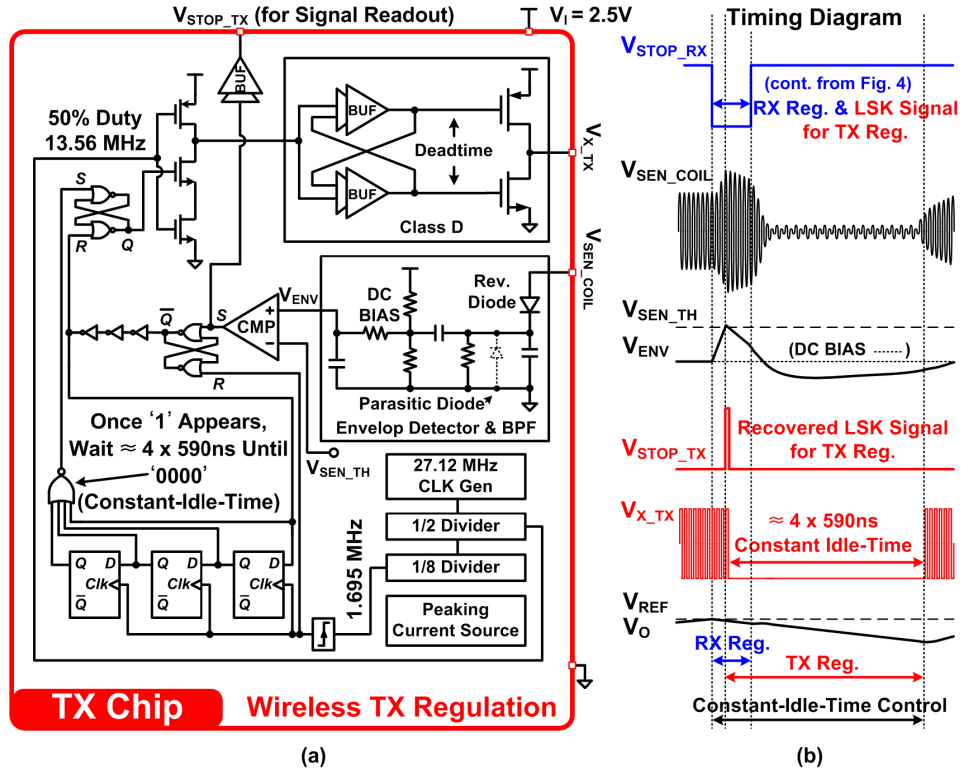


Fig. 6. (a) Detailed circuitry and (b) operation principle of the TX chip of the proposed WPT system.

### C. Operation Principle of the TX Wireless Voltage Regulation

During the RX local voltage regulation, the TX wireless voltage regulation will be triggered. Fig. 6 shows the detailed

circuitry of the TX chip, as well as the operation principle of TX wireless voltage regulation. The TX chip contains a class D amplifier switching at 13.56 MHz with 50% duty cycle,

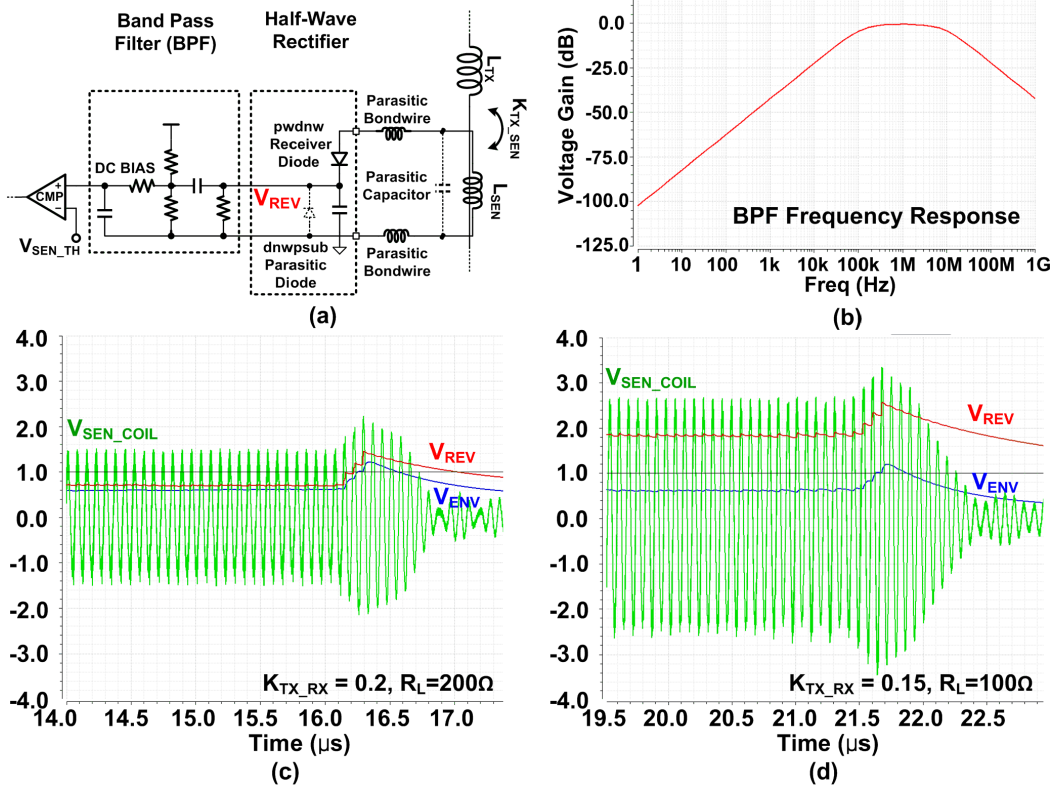


Fig. 7. (a) Half-wave envelope detector and BPF. (b) Frequency response of the BPF. The  $V_{REV}$  and AC coupled  $V_{ENV}$  with different operation conditions (c)  $K_{TX\_RX} = 0.2$ ,  $R_L = 200\Omega$  and (d)  $K_{TX\_RX} = 0.15$ ,  $R_L = 100\Omega$ .

an integrated half-wave envelope detector, and bandpass filter to recover the envelope of the sensing voltage, some DFFs, and a NOR gate to generate the  $\sim 2\text{-}\mu\text{s}$  constant-idle-time. When the  $V_{STOP\_RX}$  is triggered at the RX side indicating too much power received, the resistance difference due to the shorting inputs of the RX will be reflected to the TX. The TX coil current will thus increase, and the TX sensing coil voltage  $V_{SEN\_COIL}$  will also increase immediately. The envelope of  $V_{SEN\_COIL}$  will then be recovered inside the TX chip by the integrated envelope detector, and filtered by the BPF as  $V_{ENV}$ . When  $V_{ENV}$  triggers the threshold voltage  $V_{SEN\_TH}$ ,  $V_{STOP\_TX}$  will become high and the switching of the class D amplifier will be stopped to save power. It will stop for four clock cycles of a 1.695-MHz clock, which is roughly  $2\text{ }\mu\text{s}$ . Then, the TX will be switching again, and ends the TX wireless voltage regulation.

For this application, half-wave envelope detector is used to recover the signal. As shown in Fig. 7(a), the diode is implemented with p-well-deep-n-well diode, with a parasitic diode from the deep-n-well to substrate. The frequency response of the BPF is shown in Fig. 7(b). As shown in the red curve in Fig. 7(c) and (d), the DC level at the output of the envelope detector is variable at different operation conditions and unpredictable. So only the difference before and after the impedance change should be extracted for determination, thus the DC information is removed by an high-pass filter. Instead, a fixed bias DC level is assigned by a resistor divider, and then another low-pass filter is used to filter the high-frequency noises. During operation, the class D amplifier is

always switching at 13.56 MHz. It is divided from a 27.12-MHz internal clock, and further divided to generate the  $\sim 2\text{-}\mu\text{s}$  idle time. The idle time length  $\sim 2\text{ }\mu\text{s}$  is determined by balancing the  $V_O$  ripple and the off-chip output capacitor,  $C_{O2}$  in Fig. 3, considering the worst case output current. For example, by calculating using  $i \cdot t = C \cdot v$ , if  $C_{O2}$  is set at  $1\text{ }\mu\text{F}$ , the maximum output current is 25 mA, with 50 mV maximum  $V_O$  ripple allowance, the maximum idle time can be calculated as  $2\text{ }\mu\text{s}$ . Some simulation results at different coupling coefficient and load conditions are shown in Fig. 8.

By using the proposed constant-idle-time control, the circuitry and system complexity is significantly reduced to achieve both RX local and TX wireless voltage regulation. Only comparators, basic logic gates, DFFs and passive components are used, and they are all integrated on-chip. Because of the nature of the comparator-based operation, stability compensation is not required and fast load-transient response can be expected.

#### D. Extra Efficiency Tradeoff During the Gap Time

Although ZVS is implemented to minimize the energy lost when the RX CAC is shorted, during the gap time between RX is shorted and TX is stopped, extra energy is still generated in the TX and necessary in order to trigger the threshold and stop the TX, thus efficiency can be affected. Fortunately, after the RX regulation and  $M_{STOP}$  releases, actually part of the energy stored in the TX LC tank is still able to transfer to the load, so not all extra energy is lost. As shown in Fig. 9,

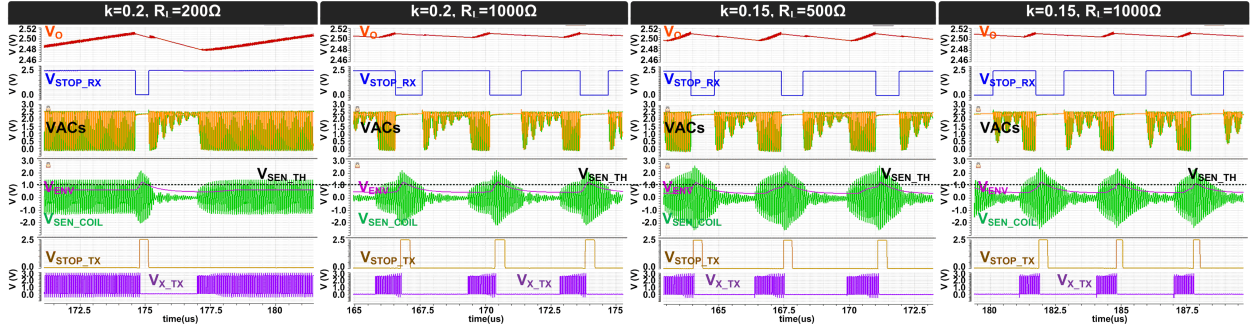


Fig. 8. Simulation waveforms at different operation conditions.

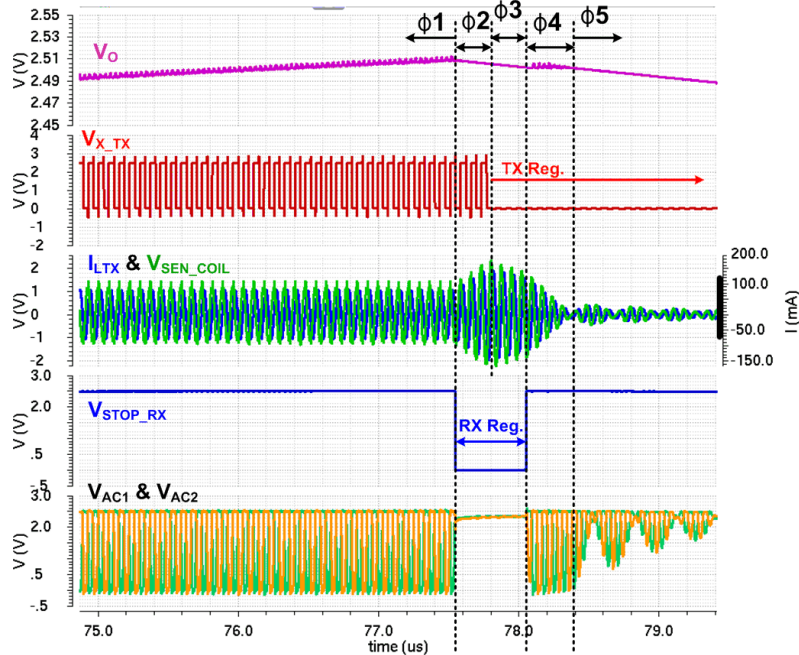


Fig. 9. Simulated waveforms with different operation phases for the explanation of extra energy during the gap between RX is shorted and TX is stopped.

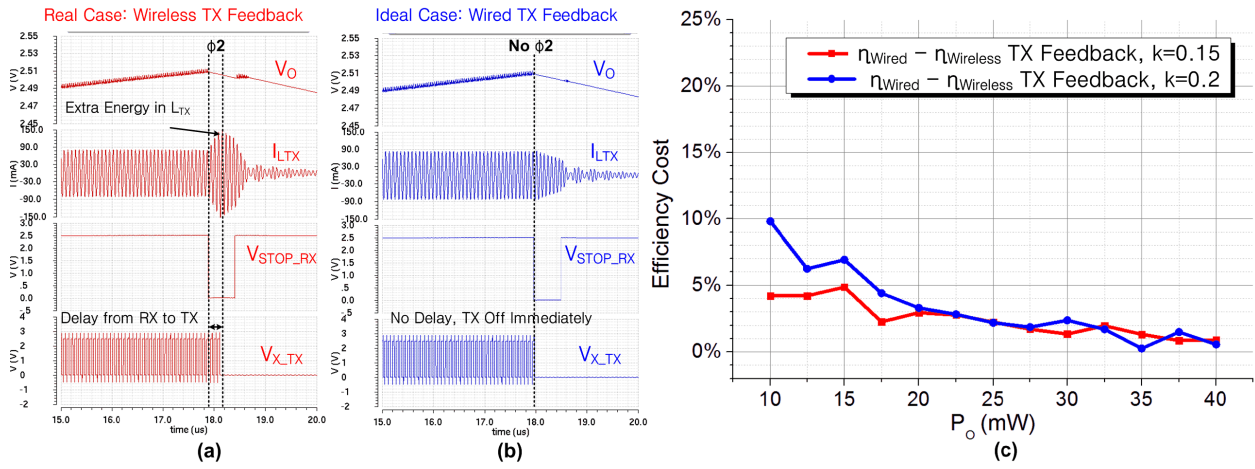


Fig. 10. Simulation setup of (a) real-case wireless TX regulation versus (b) ideal case with wired TX feedback with no delay for comparison, and (c) simulated efficiency impact.

the operation can be divided into five phases. In  $\Phi 1$ , both RX and TX are switching. In  $\Phi 2$ , RX regulation is triggered and the RX inputs are shorted. Lower reflected resistance to the TX keeps increasing the TX coil current until the TX regulation

is triggered. So the energy generated during this gap period by the TX can be counted as extra energy. If the wireless regulation link was ideal, for example, as shown in Fig. 10(b), a wire could be used to turn off the TX from the exact moment

RX is shorted without delay, there would be no extra energy generated. In  $\Phi_3$ , TX regulation is triggered and the TX stops switching. During  $\Phi_2$  and  $\Phi_3$ , the energy in the TX LC tank, including the extra energy from the delay period  $\Phi_2$  and the left energy from the original operation, is resonating inside the tank with losses due to the limited  $Q$  of the tank. Then at  $\Phi_4$ , the  $M_{STOP}$  at the RX releases, so the rest of the energy in the TX LC tank is still able to be transferred and consumed by the load. After that, in  $\Phi_5$ , the energy from the TX is used up, and the left energy in the RX LC tank is not enough to turn on the active diodes, so it just resonates in the RX LC tank and dies down due to the low  $Q_{RX}$ .

In order to extract how the extra energy lost affects the total efficiency, a simulation comparing the real case and the ideal case, as the cases shown in Fig. 10(a) and (b), is performed. Fig. 10(c) shows the simulation results at different  $k$  and power levels. The extra losses have less contribution at heavy load while more contribution at light load. This is because at light load, the output power is less thus the power losses simply have more contribution to the efficiency loss, while at the same time the RX and TX stops more frequently. This extra power loss can be considered as a tradeoff of establishing the wireless TX regulation without using any off-chip components. Please note that these losses are always included in the efficiency measurement in this paper, while in previous works [7], [8], [13], and [14], the power consumed by the active off-chip components such as DAC/MCU/decoder/controllers was not included.

#### E. Sensing Coil Design Considerations

First of all, the sensing coil is not designed to receive power, and the loading to the TX should be as small as possible to avoid affecting the efficiency. So it should be designed as a transformer without adding resonant capacitance tuned at the switching frequency [9], [13]. And it is important to design  $k_{TX\_SEN}$  and  $L_{SEN}$  large enough so that the RX shorting signal can be easily identified and recovered under different  $k_{TX\_RX}$  and loading combinations. For a parallel-resonant RX, the equivalent loading  $R_{EQ}$  reflected to the TX can be described in (1). Since, the TX regulation depends on the resistance difference between shorted and normal operation at RX, the smallest difference or worst case sensing signal level appears with smallest  $k$  and  $R_L$ . With a well-tuned LC tank, the difference of the TX coil current before and after the RX is shorted can be expressed as

$$\Delta i_{TX\_SHT} \approx \frac{V_I}{R_S + R_{EQ\_SHT}} - \frac{V_I}{R_S + R_{EQ\_MIN}} \quad (2)$$

in which  $R_S$  is the serials resistance of the TX coil,  $R_{EQ\_SHT}$  is the reflected resistance of a shorted RX, and  $R_{EQ\_MIN}$  is the worst case reflected load resistance. As shown in Fig. 11, the  $\Delta i_{TX\_SHT}$  has a ring-up time constant related to the  $Q$ -factor of the equivalent TX RLC tank in Fig. 2(e). The  $Q$ -factor can be calculated by

$$Q_{SHT} = \frac{1}{R_S + R_{EQ\_SHT}} \sqrt{\frac{L_{TX}(1 - k_{TX\_RX}^2)}{C_{TX}}} \quad (3)$$

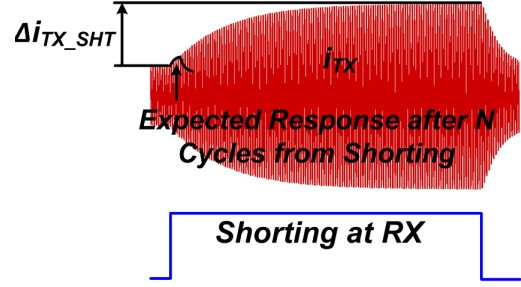


Fig. 11. Ring-up behavior illustration of TX coil current when RX is shorted.

The gap between RX is shorted and TX stops switching, which is the expected response cycles shown in Fig. 11, should be short enough to avoid wasting too much energy as discussed in Section II-D. The actual TX coil current difference after  $N$  switching cycles can be expressed as

$$\Delta i_{TX\_N} = \Delta i_{TX\_SHT} (1 - e^{-\frac{N\pi}{Q_{SHT}}}) \quad (4)$$

After that, the voltage difference on the sensing coil  $\Delta V_{SEN}$  due to  $\Delta i_{TX\_N}$  can be calculated by

$$\Delta V_{SEN} = 2\pi f_S k_{TX\_SEN} \sqrt{L_{SEN} L_{TX}} \cdot \Delta i_{TX\_N} \quad (5)$$

in which  $f_S$  is the switching frequency of 13.56 MHz. The worst case  $\Delta V_{SEN}$  should be designed larger than the sensing threshold in order to be recovered in the TX. Simulations should be performed in cadence with the designed  $k_{TX\_SEN}$  and  $L_{SEN}$  to verify the operation under possible combinations of  $k_{TX\_RX}$  and  $R_L$ .

After the design of the sensing coil, the coupling coefficient between the three coils can be extracted in HFSS, as shown in Fig. 12. The  $k_{TX\_SEN}$  is almost constant since both TX and sensing coils are fixed on the same PCB. The  $k_{RX\_SEN}$  is always much smaller than  $k_{TX\_SEN}$  since there is distance between RX and TX, and the TX coil is usually designed larger than the RX coil to allow some degrees of misalignment. Fig. 13 shows a typical-case simulation of the case I in Fig. 8. In this case,  $k_{RX\_SEN}$  is 43.5% of  $k_{TX\_SEN}$ . In the simulation setup shown in Fig. 13(a), a duplicated  $L_{SEN}$  is used to receive the signal coupled from the RX coil as  $V_{SEN\_COIL\_RX}$ , and added on to  $V_{SEN\_COIL\_TX}$  as  $V_{SEN\_COIL\_MIX}$ . The envelope of  $V_{SEN\_COIL\_MIX}$  is then extracted and filtered as  $V_{ENV\_MIX}$  to control the system. For comparison, a duplicated envelope detector and BPF is used to extract  $V_{ENV\_TX}$  from  $V_{SEN\_COIL\_TX}$ . Fig. 13(b) shows the simulation waveforms. The signal level of  $V_{SEN\_COIL\_TX}$  is much larger than  $V_{SEN\_COIL\_RX}$ . In the zoomed-in view of figure, the  $V_{SEN\_COIL\_MIX}$  almost overlaps the  $V_{SEN\_COIL\_TX}$ . There is some minor impact from the  $V_{SEN\_COIL\_RX}$  though. When RX is shorted, the  $V_{SEN\_COIL\_TX}$  increases immediately, while the  $V_{SEN\_COIL\_RX}$  decreases. This does result in about 11.7% degradation in the signal level of  $V_{ENV\_MIX}$  compared to  $V_{ENV\_TX}$ . For the worst case scenario that  $K_{RX\_SEN}$  is 60.7% of  $K_{TX\_SEN}$ , the  $V_{ENV\_MIX}$  is about 16.2% lower than  $V_{ENV\_TX}$ . However, this only introduces minor impact to the operation of the system, which would be

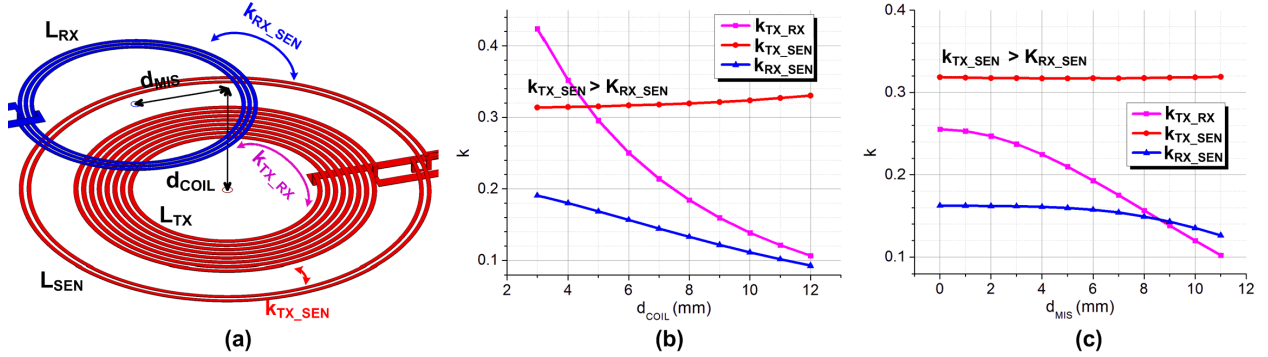


Fig. 12. (a) Illustration of the misalignment and distance and the coupling between the three coils. HFSS extracted coupling coefficient between the three coils with different (b) distance and (c) misalignment.

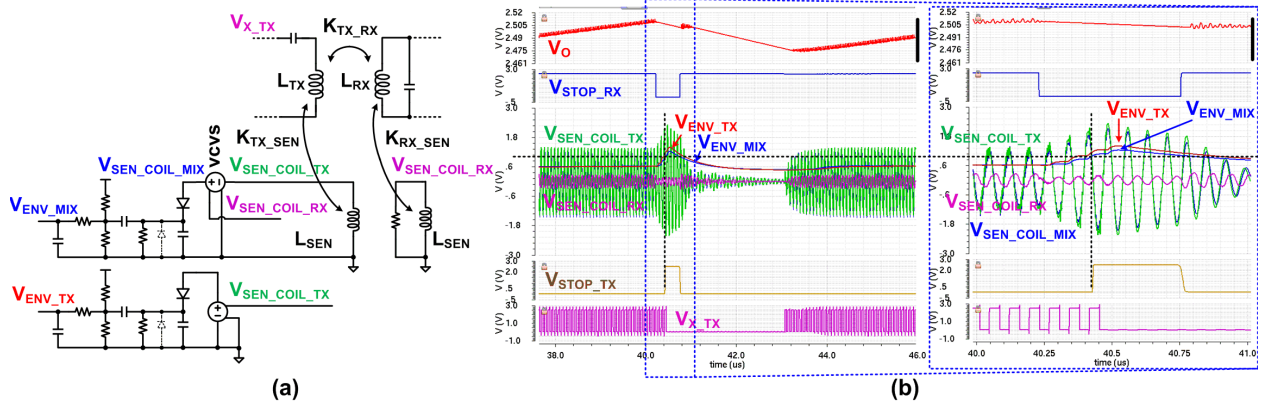


Fig. 13. (a) Simulation setup for the comparison of  $V_{SEN}$  and  $V_{ENV}$  signal levels coupled from TX and RX coils and (b) simulated waveforms with  $k_{TX_RX} = 0.2$  and  $R_L = 200 \Omega$ .

the slight increase of the gap between RX is shorted to TX is stopped. For example, if  $N$  is designed to be 3, then it may become 4 at the worst case.

In terms of power consumption of the sensing coil and related circuits, as long as the loading of the coil is small enough, the impact on the efficiency is negligible. In this design, the  $RC$  in the envelope detector is  $400 \text{ k}\Omega$  and  $5 \text{ pF}$ , the worst case efficiency impact is less than 0.5%.

#### F. Other System Design Considerations

This prototype chip is designed to supply cochlear implants with maximum power rating of around 20 to 40 mW [2], [18], [19]. With the availability of TSMC 65-nm 2.5-V I/O devices, the maximum operating voltage is 2.5 V. If higher voltage needs to be supported, for example the TX is directly supplied by an Li-Ion battery, a different process or stacking power stage [20] can be used. For the  $V_O$  at the RX, it can be regulated from 1.2 to 2.5 V, which is able to cover a wide range of different process and loading applications. For the coil selection, as the system is designed to fit into the implants, the RX coil should be small enough. It is designed to have 2-cm diameter, which is similar to [19], smaller than [16] while larger than [9]. A square RX coil is not very suitable for implants because it has relatively sharp corners, so round coil is used [9], [13]. Although flexible printed circuit (FPC)

usually comes with thinner layer of copper and thus lower quality factor, but the flexibility makes it more suitable for implants. As a result, a round, 2-cm diameter coil fabricated on FPC is designed based on the instructions in [21]. For the inductance of the RX coil, it is designed to roughly resonate with the capacitance on the active rectifier with some tunable margin. In this paper, the active rectifier design in [17] is reused with the RX local regulation circuits added to adapt with the new constant-idle-time control. The total capacitance including the extracted parasitic capacitance of power PMOS and the integrated MOM and MIM resonant capacitances is about 330 pF. Considering  $\pm 20\%$  process variation, it could be from 264 to 396 pF. So the RX coil is designed to roughly resonate with 396 pF to be around 350 nH. For the TX coil, it is designed to be a bit larger than that of the RX coil to allow misalignment. It is designed with traditional PCB since the TX is external. For the inductance of TX coil, simulation can be used to make sure the link gain is enough with different  $k$  and loading combinations. HFSS can be used to extract the coupling coefficient, inductance and Q-parameters for cadence simulation.

#### G. Real-Time Delay Calibration in the RX Active Rectifier

As mentioned in Section II-A, the real-time delay calibration is also implemented in the system for higher efficiency.

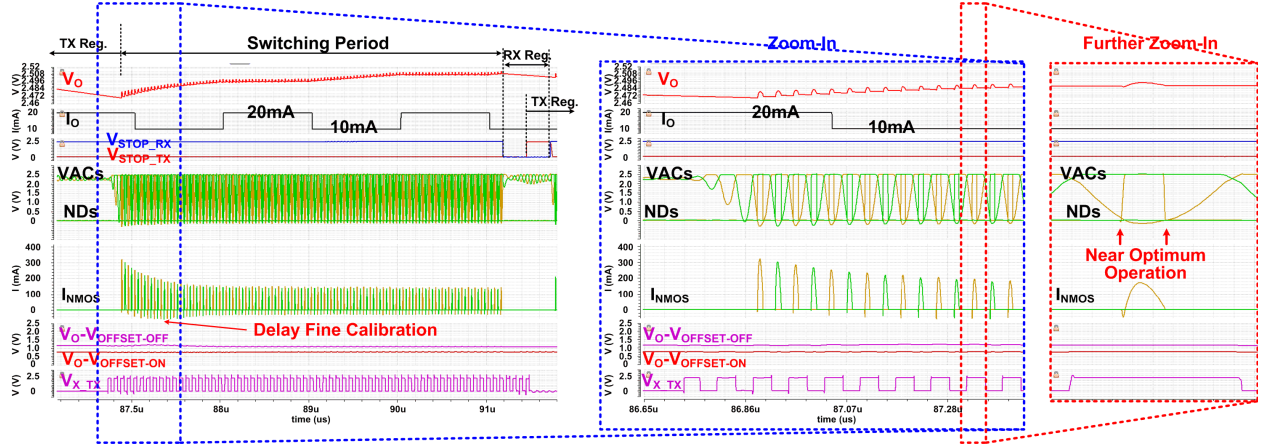


Fig. 14. Simulated behaviors of the real-time delay compensation of the RX active rectifier in the complete system with RX and TX voltage regulation.

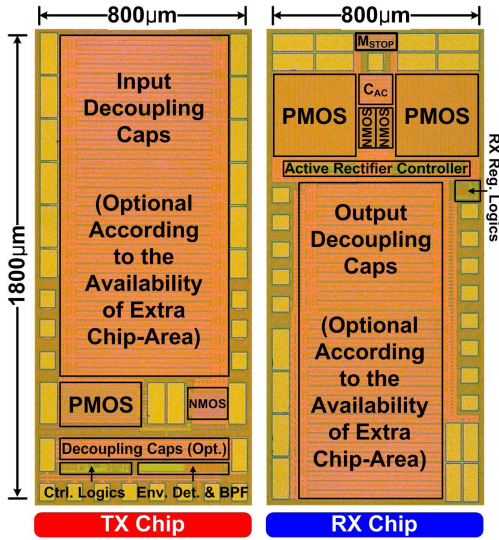


Fig. 15. Chip photographs of the TX and RX chips.

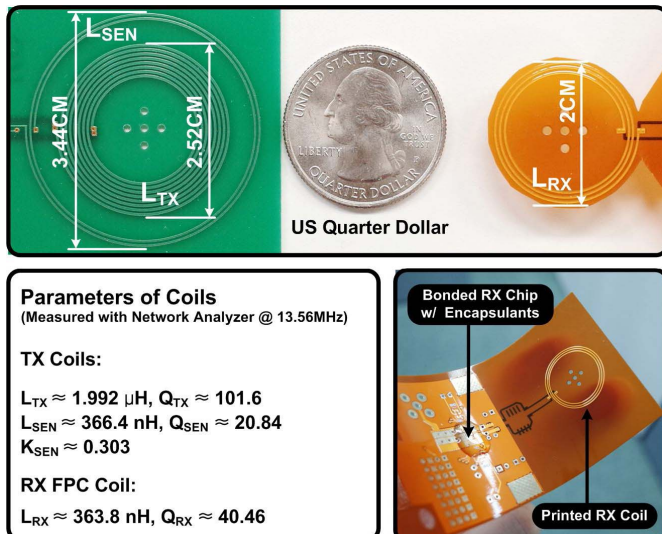


Fig. 16. Parameters of the TX coils on PCB and the RX coil on FPC.

Detailed operation principle can be found in [17]. Circuit delays depend on process, voltage, temperature, and the slew rate when  $V_{AC}$  crosses zero voltage. These conditions will

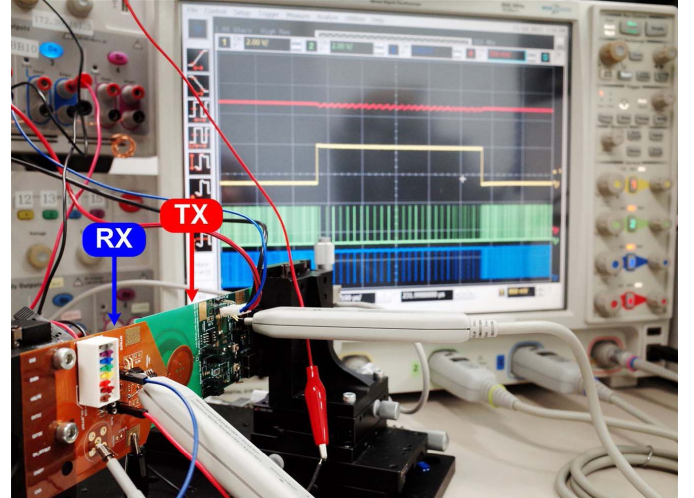


Fig. 17. Measurement setup during a live load transient.

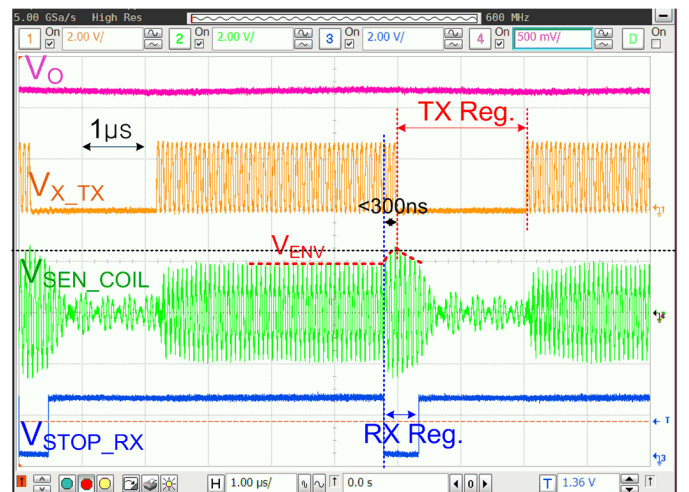


Fig. 18. Measured waveforms showing the constant-idle-time operation with TX and RX voltage regulation.

not change rapidly and significantly during the operation. So the delay calibration loops will not have large transients and require long settling between different states, only some real-time fine-tuning to maintain the near-optimal operation. Fig. 14 shows the waveforms of how the delay calibration

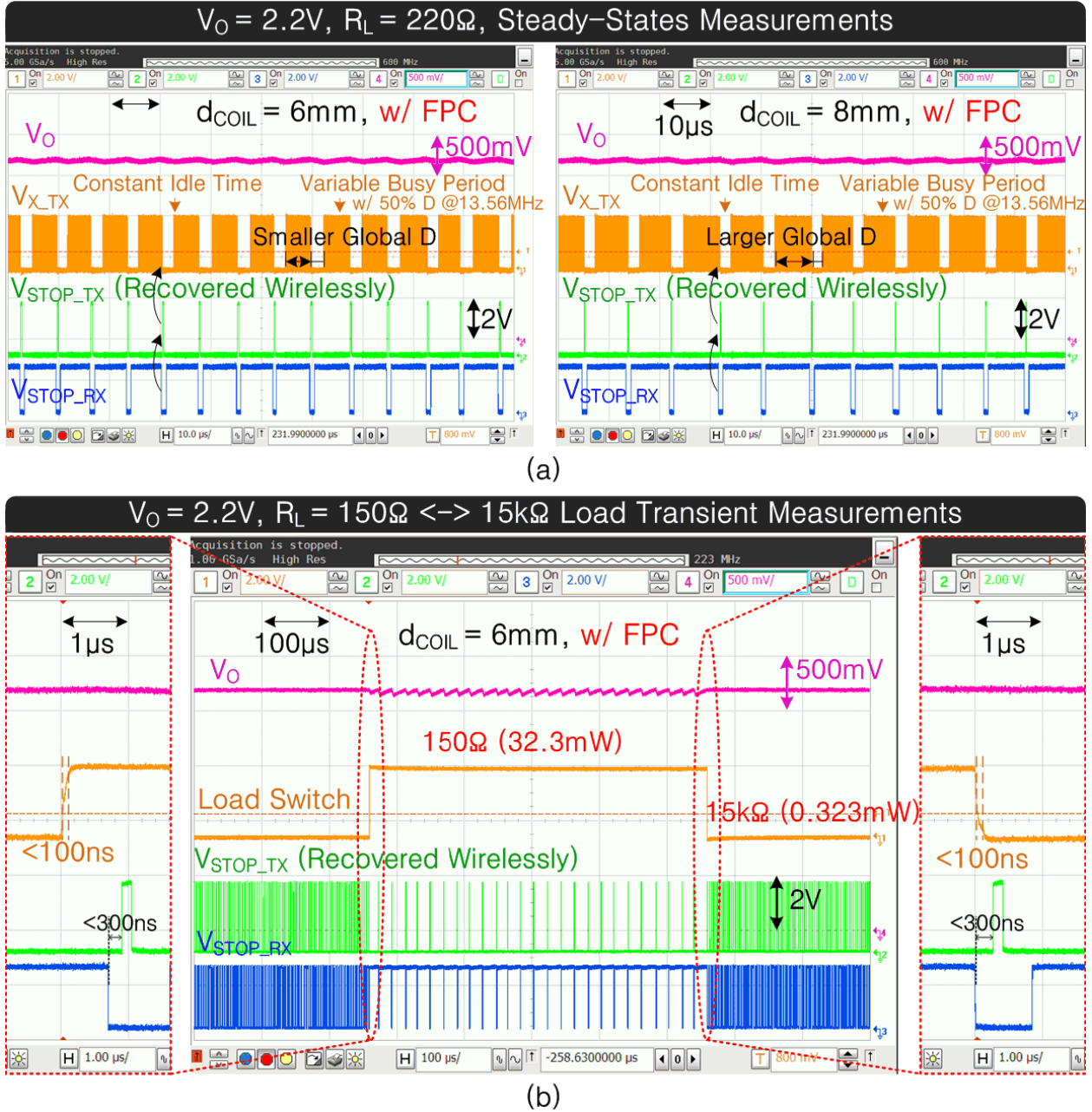


Fig. 19. Measured waveforms at (a) steady state and (b) during load transients.

loops behave in the complete system with TX and RX voltage regulation and switching load. In the simulation,  $I_O$  is continuously switching between 10 and 20 mA. But due to the large 1- $\mu\text{F}$   $C_{O2}$  and the minor difference in circuit delays, the difference in the NMOS current is barely noticeable. On the other hand, when both TX and RX resumes switching from the idle period, the currents running through the NMOSs that charges the output capacitors ( $C_{O1}$  and  $C_{O2}$ ) is much higher than normal operation because the  $V_O$  is at the lowest. In this case, the previous calibrated offset currents are off the most, but the error is still small enough not to create much difference in reverse current. The real-time calibration loops keep fine-tuning the offsets, and soon settle after a few cycles at the near-optimum condition.

### III. MEASUREMENT RESULTS

Both the TX and RX chips are fabricated in TSMC 65 nm and occupy two blocks of  $0.8 \times 1.8 \text{ mm}^2$ , as shown in Fig. 15. The chip areas are dominated by the optional input and output decoupling capacitors, which are 5 and 4.2 nF, respectively, because of the extra areas during chip fabrication. The effective circuit areas at both TX and RX, such as the power stages and control circuits, only consume 0.276 and 0.464  $\text{mm}^2$ , respectively. The detailed measured parameters of the coils are shown in Fig. 16. Fig. 17 shows the measurement setup during a live load transient. The constant-idle-time operation with RX and TX regulations and  $V_{SEN\_COIL}$  signals is shown in the measured waveforms in Fig. 18. Measured waveforms at steady state and during load transients

TABLE I  
COMPARISON WITH STATE OF THE ART

	[16] ISSCC'17	[13] TCAS-I'05	[9] JSSC'15	[14] ISSCC'15	[7] ISSCC'13	[8] JSSC'13	[11] ISSCC'12	This Work
System Level on Silicon	Both TX & RX	Both TX & RX	Both TX & RX	Both TX & RX	RX Only	RX Only	Both TX & RX	Both TX & RX
Tech.	CMOS 0.18μm	CMOS 1.5um	CMOS 0.35μm	CMOS 0.35μm	BCD 0.13μm	BCD 0.35μm	HVCMOS 0.18μm	CMOS 65nm (I/O Devices)
RX Vo	2.1-2.5V	14V	3.6V	3.7V	4.2-5.8V	5V	15V	1.2-2.5V
POUT(MAX)	18mW	250mW	102mW	234mW	6W	6W	0.52W	49.4mW (PCB [6]) 38.4mW (FPC)
Freq. (MHz)	10.4-13.56	1	13.56	13.56	6.78	6.78	13.56	13.56
Reg. Site	TX & RX (LDO)	TX & RX (LDO)	TX & RX (Rec.)	TX & RX (Rec.)	TX & RX (Buck/LDO)	TX & RX (Rec.)	TX	TX & RX (Rec.)
TX Reg. Data Link	Not Required	Wireless LSK	Wireless LSK	Wireless LSK	Wireless 2.4GHz	Wire	Wire	Wireless LSK
Loop Stability Compensation	N/A	Required	Required (Dominant-Pole)	Required (Dominant-Pole)	Required (Pole-Zero)	Required (Dominant-Pole)	Required	Not Required (CMP-Based)
Off-Chip Components Required for TX Reg.	None	Inductor (for TX Buck); Buck Converter and Controller; Envelop Detector; Data Decoder	RX Digital Ctrlr.; TX Pulse Ctrlr.; Decoder; Diodes	Inductor (for TX Buck); DAC & its Ctrlr.; Data Receiver; BPF	Comm. Module; MCU	MCU; Wire	Wire	None
ΔVo/Vo <sup>1</sup>	N/A	0.7% <sup>2</sup>	3.1% <sup>2</sup>	4.38% <sup>2</sup>	N/A	3.2% <sup>2</sup>	2.7% <sup>2</sup>	2% <sup>3</sup> (@2.5V) 4.1% <sup>3</sup> (@1.2V)
Load Reg. <sup>4</sup>	N/A	N/A	N/A	2.06mV/mA	N/A	N/A	N/A	0.9mV/mA
Load-Tran. Recovery Time	N/A	40ms	130μs	2ms	N/A	500μs	30μs	0μs
RX Coil Material	PCB	N/A	PCB	PCB	N/A	N/A	PCB	PCB [6] FPC
Peak Total Effi. (@ dCOIL)	73.7% (N/A)	65.8% <sup>5</sup> (7mm)	50% <sup>5</sup> (3mm)	62.4% <sup>5</sup> (3mm)	N/A	55% <sup>5</sup> (N/A)	50% (5mm)	70.6% (6mm) 69% (6mm)

<sup>1</sup> Including the ΔVo due to steady-state Vo ripples and over-/under-shoot voltages during load-transients.

<sup>2</sup> Limited by the over-/under-shoot voltages during load-transient and is limited by system bandwidth.

<sup>3</sup> Limited by the voltage ripple at steady-state with heavy load, can be further improved by more Co.

<sup>4</sup> Load Regulation represents the capability of maintaining a constant steady-state Vo under different loadings.

<sup>5</sup> Power consumed by the off-chip active components, such as controllers, decoders, DAC and MCU, is not included.

are shown in Fig. 19(a) and (b), respectively. As shown in Figs. 18 and 19 (a), the VSTOP\_TX is successfully recovered wirelessly inside the TX chip when VSTOP\_RX is triggered at the RX side. It stops more frequently with  $d_{COIL} = 6$  mm compared  $d_{COIL} = 8$  mm, which simply represents that more power is received at  $d_{COIL} = 6$  mm. The effective global duty cycle ( $D$ ) can be defined as the busy period divided by the sum of busy and idle period. When coupling condition becomes weaker or loading becomes heavier, the TX stops less frequently and thus the global  $D$  increase, until the TX never stops and the global  $D$  finally reaches 1. Fig. 19(b) shows the waveforms when the load transients between 32.3 and 0.323 mW (two decades) with a time-step less than 100 ns. The load-transient response is very different from the conventional works with under-/over-shoots at  $V_O$  [9], [13], [14]. Technically, this paper does not need to respond to a load transient and recover because the constant-idle-time control is comparator-based and only shuts off the RX and TX when  $bV_O$  exceeds  $V_{REF}$ . The load-transient response is thus not limited by the system bandwidth and loop stability as other works do. For example, within the power capability of the TX, if the load suddenly switches from light to heavy, the TX and RX just stop less frequently from the time load-transient happens. So the over-/under-shoot voltages during load transients in Fig. 19 are unnoticeable, and the response is instant. Instead, the fluctuation of  $V_O$  ( $\Delta V_O$ ) during operation is limited by the steady-stage ripple at heavy load. It is simply a tradeoff with the off-chip  $C_O$  as discussed in Section II-C.

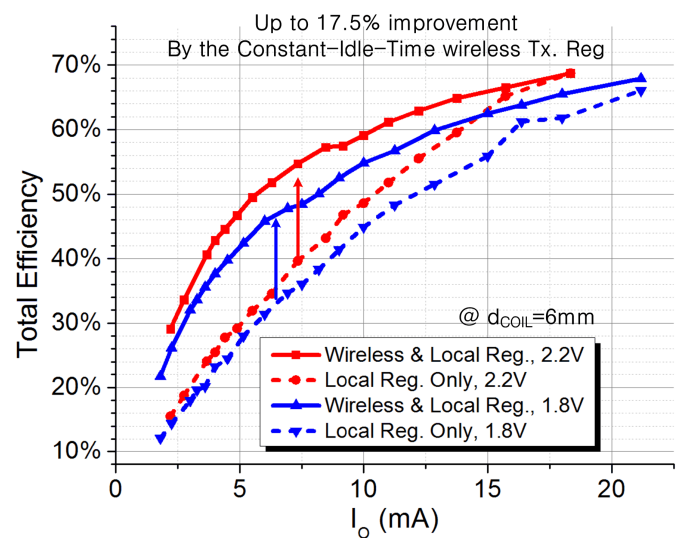


Fig. 20. Measured efficiency versus load current at 2.2 and 1.8 V, with and without the wireless TX voltage regulation by the constant-idle-time control.

Reducing the  $C_O$  due to cost or limited package space will result in higher  $V_O$  ripple. However, general purpose ceramic capacitors can be tiny while not very costly. For example, the Murata X5R series 1 μF can be as small as  $0.5 \times 0.25$  mm, which is even smaller than the chip.

Fig. 20 shows the measured total efficiency versus load current. With the constant-idle-time controlled wireless TX

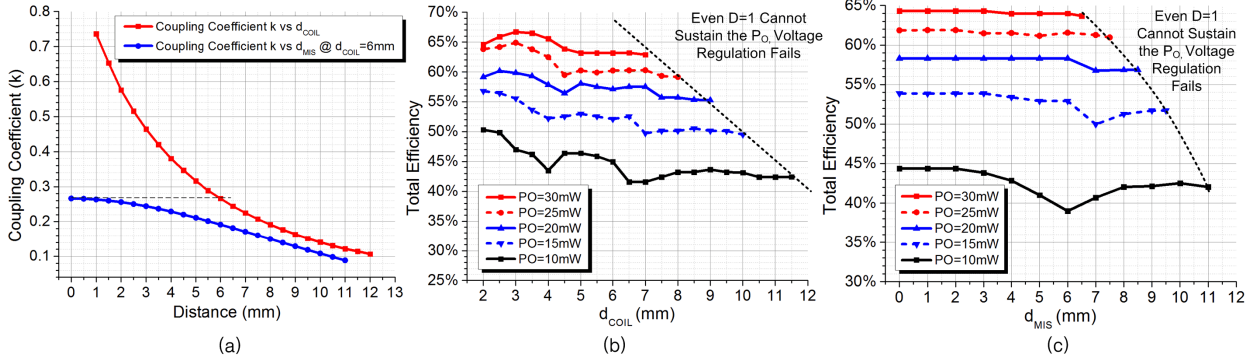


Fig. 21. Measurement results of (a) coupling coefficient between RX and TX coils with different misalignment and distance conditions; the total efficiency with different power at (b) different  $d_{COIL}$  at  $d_{MIS} = 0\text{ mm}$  and (c) different  $d_{MIS}$  at  $d_{COIL} = 6\text{ mm}$ .

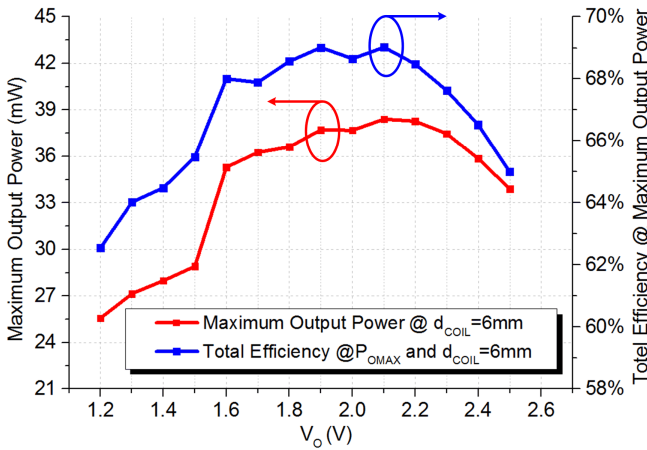


Fig. 22. Measured maximum output power and the efficiency at maximum output power with  $V_O$  regulated at different voltages.

voltage regulation enabled, the efficiency improvement at normal operation is up to 17.5% compared with local RX voltage regulation only. To further demonstrate the performance of the proposed WPT system under various situations, the coupling coefficient between coils, and the total efficiency with different coil distances and misalignment conditions are measured, as shown in Fig. 21. The measurement is done until the  $V_O$  fails to regulate, as the boundary marked in Fig. 21(b) and (c). Beyond the boundary, both RX and TX will switch continuously with  $D = 1$ . The operation, and efficiency and voltage roll-off characteristics are similar to other WPT systems. The maximum output power with the total efficiency is also measured with different regulated  $V_O$ , as shown in Fig. 22. Table I gives a comparison summary with state-of-the-art works. Comparing to previous works, this design achieves a higher total efficiency, a faster load-transient recovery time, and a higher level of integration with a more straightforward system and circuitry design.

#### IV. CONCLUSION

In this paper, a fully integrated wireless constant-idle-time control technique is proposed to achieve both RX local and TX wireless voltage regulation. Thanks to the proposed comparator-based constant-idle-time control technique, the system and circuitry design complexity is significantly

reduced, and no off-chip components or wires that were required in previous designs are used. In the measurement, up to 17.5% end-to-end total efficiency improvement is observed with the TX voltage regulation by the wireless constant-idle-time control enabled. A 69% peak total efficiency with FPC RX coil and an instant load-transient response are also achieved.

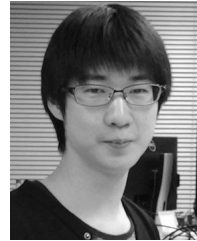
#### REFERENCES

- [1] P. T. Bhatti and K. D. Wise, "A 32-site 4-channel high-density electrode array for a cochlear prosthesis," *IEEE J. Solid-State Circuits*, vol. 41, no. 12, pp. 2965–2973, Dec. 2006.
- [2] S. Guo and H. Lee, "An efficiency-enhanced CMOS rectifier with unbalanced-biased comparators for transcutaneous-powered high-current implants," *IEEE J. Solid-State Circuits*, vol. 44, no. 6, pp. 1796–1804, Jun. 2009.
- [3] K. Chen, Y. K. Lo, Z. Yang, J. D. Weiland, M. S. Humayun, and W. Liu, "A system verification platform for high-density epiretinal prostheses," *IEEE Trans. Biomed. Circuits Syst.*, vol. 7, no. 3, pp. 326–337, Jun. 2013.
- [4] H. G. Graf *et al.*, "High dynamic range CMOS imager technologies for biomedical applications," *IEEE J. Solid-State Circuits*, vol. 44, no. 1, pp. 281–289, Jan. 2009.
- [5] W. Biederman *et al.*, "A 4.78 mm<sup>2</sup> fully-integrated neuromodulation soc combining 64 acquisition channels with digital compression and simultaneous dual stimulation," *IEEE J. Solid-State Circuits*, vol. 50, no. 4, pp. 1038–1047, Apr. 2015.
- [6] C. Huang, T. Kawajiri, and H. Ishikuro, "A wireless power transfer system with enhanced response and efficiency by fully-integrated fast-tracking wireless constant-idle-time control for implants," in *Proc. IEEE Symp. VLSI Circuits*, Jun. 2016, pp. 1–2.
- [7] K.-G. Moh *et al.*, "A fully integrated 6 W wireless power receiver operating at 6.78 MHz with magnetic resonance coupling," in *IEEE Int. Solid-State Circuits Conf. (ISSCC) Dig. Tech. Papers*, Feb. 2013, pp. 1–3.
- [8] J.-H. Choi, S.-K. Yeo, S. Park, J.-S. Lee, and G.-H. Cho, "Resonant regulating rectifiers (3R) operating for 6.78 MHz resonant wireless power transfer (RWPT)," *IEEE J. Solid-State Circuits*, vol. 48, no. 12, pp. 2989–3001, Dec. 2013.
- [9] X. Li, C.-Y. Tsui, and W.-H. Ki, "A 13.56 MHz wireless power transfer system with reconfigurable resonant regulating rectifier and wireless power control for implantable medical devices," *IEEE J. Solid-State Circuits*, vol. 50, no. 4, pp. 978–989, Apr. 2015.
- [10] L. Cheng, W.-H. Ki, T.-T. Wong, T.-S. Yim, and C.-Y. Tsui, "A 6.78 MHz 6 W wireless power receiver with a 3-level  $1 \times / \frac{1}{2} \times / 0 \times$  reconfigurable resonant regulating rectifier," in *IEEE Int. Solid-State Circuits Conf. (ISSCC) Dig. Tech. Papers*, Jan./Feb. 2016, pp. 376–377.
- [11] R. Shinoda, K. Tomita, Y. Hasegawa, and H. Ishikuro, "Voltage-boosting wireless power delivery system with fast load tracker by  $\Delta\Sigma$ -modulated sub-harmonic resonant switching," in *IEEE Int. Solid-State Circuits Conf. (ISSCC) Dig. Tech. Papers*, Feb. 2012, pp. 288–290.
- [12] R. R. Harrison *et al.*, "A low-power integrated circuit for a wireless 100-electrode neural recording system," *IEEE J. Solid-State Circuits*, vol. 42, no. 1, pp. 123–133, Jan. 2007.

- [13] G. Wang, W. Liu, M. Sivaprakasam, and G. A. Kendir, "Design and analysis of an adaptive transcutaneous power telemetry for biomedical implants," *IEEE Trans. Circuits Syst. I, Reg. Papers*, vol. 52, no. 10, pp. 2109–2117, Oct. 2005.
- [14] X. Li, C.-Y. Tsui, and W.-H. Ki, "Wireless power transfer system using primary equalizer for coupling- and load-range extension in bio-implant applications," in *IEEE Int. Solid-State Circuits Conf. (ISSCC) Dig. Tech. Papers*, Feb. 2015, pp. 1–3.
- [15] C.-S. Wang, G. A. Covic, and O. H. Stielau, "Power transfer capability and bifurcation phenomena of loosely coupled inductive power transfer systems," *IEEE Trans. Ind. Electron.*, vol. 51, no. 1, pp. 148–157, Feb. 2004.
- [16] J. Pan, A. A. Abidi, D. Rozgić, H. Chandrakumar, and D. Marković, "An inductively-coupled wireless power-transfer system that is immune to distance and load variations," in *IEEE Int. Solid-State Circuits Conf. (ISSCC) Dig. Tech. Papers*, Feb. 2017, pp. 382–383.
- [17] C. Huang, T. Kawajiri, and H. Ishikuro, "A near-optimum 13.56 MHz CMOS active rectifier with circuit-delay real-time calibrations for high-current biomedical implants," *IEEE J. Solid-State Circuits*, vol. 51, no. 8, pp. 1797–1809, Aug. 2016.
- [18] H.-M. Lee and M. Ghovanloo, "An integrated power-efficient active rectifier with offset-controlled high speed comparators for inductively powered applications," *IEEE Trans. Circuits Syst. I, Reg. Papers*, vol. 58, no. 8, pp. 1749–1760, Aug. 2011.
- [19] Y. Lu, X. Li, W.-H. Ki, C.-Y. Tsui, and C. P. Yue, "A 13.56 MHz fully integrated 1X/2X active rectifier with compensated bias current for inductively powered devices," in *IEEE Int. Solid-State Circuits Conf. (ISSCC) Dig. Tech. Papers*, Feb. 2013, pp. 66–67.
- [20] X. Liu, C. Huang, and P. K. T. Mok, "Dynamic performance analysis of 3-level integrated buck converters," in *Proc. IEEE Int. Symp. Circuits Syst.*, May 2015, pp. 2093–2096.
- [21] U.-M. Jow and M. Ghovanloo, "Design and optimization of printed spiral coils for efficient transcutaneous inductive power transmission," *IEEE Trans. Biomed. Circuits Syst.*, vol. 1, no. 3, pp. 193–202, Sep. 2007.

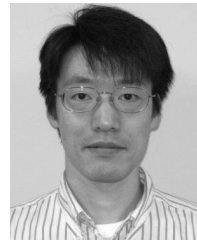


**Cheng Huang** (S'11–M'14) received the B.Eng. degree in information science and engineering from Zhejiang University, Hangzhou, China, in 2008, and the Ph.D. degree in electronic and computer engineering from the Hong Kong University of Science and Technology, Hong Kong, in 2014. From 2014 to 2016, he was a Research Scientist with the Ishikuro Laboratory, Electronics and Electrical Engineering, Keio University, Yokohama, Japan. In 2016, he joined Broadcom, San Jose, CA, USA, as an IC Design Engineer. His current research interests include power management and analog/mixed-signal IC designs.



**Toru Kawajiri** (S'15–M'16) received the B.S. and M.S. degree in electronics and electrical engineering from Keio University, Yokohama, Japan, in 2013 and 2015, respectively, where he is currently pursuing the Ph.D. degree with the Ishikuro Laboratory, Electronics and Electrical Engineering.

His current research interests include wireless power transfer systems and power management integrated circuits.



**Hiroki Ishikuro** (M'06) received the B.S., M.S., and Ph.D. degrees in electrical engineering from the University of Tokyo, Tokyo, Japan, in 1994, 1996, and 1999, respectively.

In 1999, he joined the System LSI Research and Development Center, Toshiba Corp., Kawasaki, Japan, where he was involved in the development of CMOS RF and mixed-signal circuits for wireless interface chips. In 2006, he joined the Department of Electrical Engineering, Keio University, Yokohama, Japan, as an Assistant Professor, where he focused on high-speed inductive-coupling links for 3-D chip integration and noncontact connector. He is currently a Professor with Keio University, and focuses on the mixed-signal circuit and system designs for extremely low-power interfaces.

Dr. Ishikuro is a member of the Technical Program Committee for the Symposium on VLSI Circuits.